Optik - International Journal for Light and Electron Optics 250 (2022) 168328

Contents lists available at ScienceDirect

Optik

journal homepage: www.elsevier.com/locate/ijleo

Multifunctional optoelectronic device based on liquid crystal selectively filled flat-plate photonic crystal fiber

Tiesheng Wu [a,b,c], Dan Yang [b,*], Zhizhui Liu [b], Zuning Yang [b], Weiping Cao [b], Yiping Wang [a,c,**]

[a] *Key Laboratory of Optoelectronic Devices and Systems of Ministry of Education and Guangdong Province, Shenzhen University, Shenzhen 518060, China*

[b] *Guangxi Key Laboratory of Wireless Broadband Communication and Signal Processing, School of Information and Communication, Guilin University of Electronic Technology, Guilin 541004, China*

[c] *Key Laboratory of Optoelectronic Devices and Systems of Ministry of Education and Guangdong Province, College of Optoelectronic Engineering, Shenzhen University, Shenzhen 518060, China*

A R T I C L E I N F O

Keywords:
Photonic crystal fiber
Liquid crystal
Voltage sensing

A B S T R A C T

To reduce the saturation voltage of fiber filter and improve the sensitivity of voltage sensing, we propose and numerically demonstrate a multifunctional optoelectronic device with a flat-plate photonic crystal fiber structure in this paper. One of the air holes is selectively filled with liquid crystal, and the upper and lower planes of the fiber are plated with gold films to form electrodes. Based on the applied voltage, the coupling wavelength of the core fundamental mode and filling mode is adjusted. This structure can realize the functions of tunable filtering and external voltage sensing. In addition, the metal film is close enough to the fiber core to enable coupling between the core waveguide mode and the surface plasmon resonance mode. Thus, the external RI can be measured. The measurements of the voltage and refractive index of the device are independent of each other, thus realizing a simultaneous measurement of the two parameters. We used the finite element method to investigate its photoelectric characteristics systematically. When the thickness of the plate fiber is 18 μm, as a fiber filter, the applied saturation voltage decreases from 2900 V (photonic crystal fiber with a conventional structure) to 650 V, and the threshold voltage decreases from 45 to 8 V. When used as a voltage sensor, the voltage sensitivity is improved from 0.025 to 0.117 nm/V. As a dual-parameter sensor for simultaneously measuring the voltage and RI, the RI sensitivity is 2700 nm/RIU. Evidently, the superior performance of the proposed structure renders it a high application value in the fields of optical fiber sensing and communication.

1. Introduction

Photonic crystals, which were first proposed in 1987, have the most promising applications in optical fiber technologies. It involves fibers with periodic microstructures (they are usually composed of air holes with silica as background material). This type of optical

* Corresponding author.

** Corresponding author at. Key Laboratory of Optoelectronic Devices and Systems of Ministry of Education and Guangdong Province, Shenzhen University, Shenzhen 518060, China.

E-mail addresses: dyang_guet@163.com (D. Yang), ypwang@szu.edu.cn (Y. Wang).

https://doi.org/10.1016/j.ijleo.2021.168328
Received 13 September 2021; Received in revised form 30 October 2021; Accepted 9 November 2021
Available online 13 November 2021

fiber is usually called photonic crystal fiber (PCF) and has been studied and used by many scholars. In 1996, Knight et al. successfully prepared PCF for the first time [1], signalling a breakthrough in optical fiber technology. PCFs have shown excellent market application value in optical fiber communication and sensing fields owing to their flexible structural design, corrosion resistance, light texture, anti-electromagnetic interference property, and low loss. In addition, by selectively filling the air holes of PCF with materials, its optical properties can be further adjusted, and some new functions can be realized. For example, materials, such as precious metals [2], liquids [3], polymers [4], or liquid crystals (LCs) [5–8], can be filled into the air holes of PCF to adjust its transmission and polarization properties. Among these filling materials, LC is of particular interest because its refractive index (RI) can be adjusted by voltage or temperature. So PCFs with LC filling can be designed into various optical devices, such as polarization [7], converters [9], modulators [10], filters [11], optical switches [12], interferometers [13], and sensors [14]. In 2002, Fokine et al. proposed an integrated fiber Mach–Zehnder interferometer for electro-optic switching that consisted of a single twin-core fiber with two internal electrodes [15]. In 2007, Yu et al. designed a nanosecond switching of fiber Bragg gratings which is short length , low loss and all-spliced high-speed wavelength switching [16]. In 2017, Jiang et al. proposed an ultra-wideband single-polarization filter by filling the core with liquid crystal [17]. In the same year, Yang et al. proposed and experimentally demonstrated an electrically tunable whispering gallery mode microresonator based on the HF-etched microstructured optical fiber infiltrated with nematic LCs which has a wavelength sensitivity of 0.01 nm/V for a $TM^1{}_{169}$ mode [18]. At the same time, Azab et al. proposed a surface plasmon resonance (SPR) multifunctional biosensor with LC selectively filled PCFs, exhibiting a RI and temperature sensitivity up to 3700 nm/RIU and 5 nm/℃, respectively [19]. In 2019, Tatiana et al. designed the first tunable whisper gallery mode (WGM) photonic device based on the inner electrode side hole microstructured fiber (SH-MOF), where the WGM quality factor of the device is not significantly reduced during the tuning process [20]. In the same year, Cardona et al. proposed a tunable mode conversion device based on an LC-filled PCF for the wavelength range of 1278–1317 nm [21]. In 2020, Lu er al. proposed a tunable optofluidic liquid metal core microbubble resonator, where the optical mode was thermally tuned (>3 nm) over a full free spectral range [22]. Abdelaal et al. reported and analyzed the dispersion compensation of a dual-core LC-filled PCF with an ultra-high negative dispersion of 289,118 ps/nm km and good temperature adjustability [23]. In 2021, Nelson et al. proposed a thermo-optically tunable polarization beam splitter based on selectively gold-filled dual-core PCL with integrated electrodes which has a bandwidth of 9 nm , a high extinction ratio of −83.2 dB and tuning sensitivities of −67 and 66 pm/℃ when the internal electrodes are arranged horizontally and vertically, respectively [24]. In the same year, Mahmoud et al. reported a tunable LC asymmetric dual-core PCF mode converter, which has a compact device length of 403.6 μm at $\lambda = 1.3$ μm and temperature adjustability [25]. Tian et al. proposed a small multiband thermo-optical switch containing two influential communication bands, with an extinction ratio of up to 30 dB within the bandwidth range [26]. However, these reported optoelectronic devices require a relatively high external modulation voltage, limiting their application in real environments.

PCFs with a periodic air holes arrangement are highly competitive for SPR sensing applications owing to their flexible structural characteristics. When the core mode and the surface plasmon polariton (SPP) mode meet the phase-matching condition, SPR will be excited, which is manifested by the peak loss of the core mode. Among the SPR sensors developed, the D-shaped PCF-SPR sensor is the most popular. In 2014, An et al. proposed an SPR sensor based on D-shaped PCF, which showed an average RI sensitivity of 2000 nm/RIU [27]. Further, on this basis, Chen et al. demonstrated an ultra-wideband polarization filter based on multiple resonances between the core mode and the SPP mode [28]. In 2016, Dash et al. designed a D-shaped PCF sensor with a 5200 nm/RIU sensitivity in the near-infrared range [29]. Liu et al. reported an asymmetric double D-shaped PCF SPR sensor with a RI resolution of 6.82×10^{-6} RIU [30]. In our previous work [31], we conducted a comprehensive analysis of the sensing performance of the D-shaped PCF. Most of the previously reported SPR sensors can only detect a single parameter, but there is often more than one parameter change in the application environment. Therefore, it is necessary to research multi-parameter sensing technology.

In this work, we developed a multifunctional optical device based on LC selectively filled flat-plate PCF. Considering that selective filling of the air holes can help adjust the optical characteristics of PCFs and that silica is a nonpolarized material, the modulation voltage can be reduced by the plate structure, and the gold-plated films on the plate can be used not only as electrodes but also as

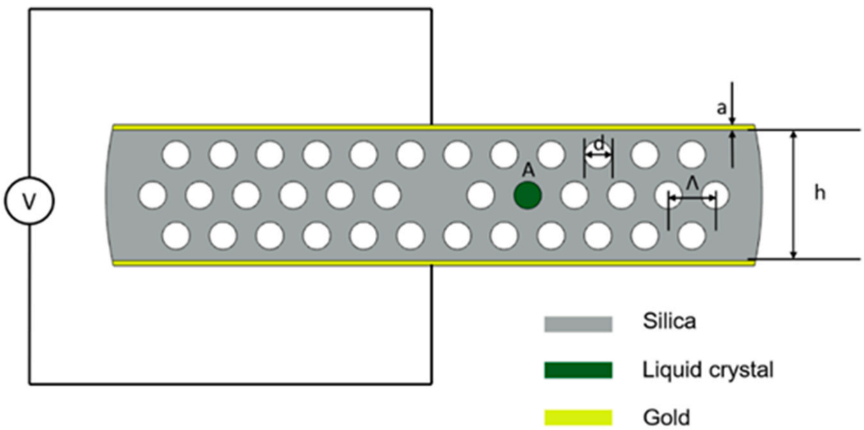

Fig. 1. Structural diagram of the proposed optoelectronic device based on LC selectively filled flat-plate PCF.

channels for SPR excitation. The electro-optical characteristics were numerically analyzed using COMSOL Multiphysics with perfect match layers (PMLs) boundaries. We systematically analyzed the influences of the thickness of the flat-plate PCF, the diameter of the air holes, the duty ratio, the thickness of the gold nanofilm, and the temperature on the loss spectrum. The simulation results showed that the above parameters significantly affect the coupling strength of the core fundamental mode and the mode in the LC-filled holes. Except for the duty ratio, the other parameters influenced the voltage sensitivity, particularly the plate thickness. However, only the thickness of the plate and the diameter of the air holes filled with the LC had a significant effect on the saturation voltage. Compared with the LC-filled voltage sensor reported in [32], which requires a saturation voltage of approximately 2525 V, the flat-plate PCF model with the selective LC filling proposed in this paper can effectively achieve lower voltage measurements. When the plate thickness is 18 μm, the applied saturation voltage decreases from 2900 V to 650 V, and the voltage sensitivity increases from 0.025 to 0.117 nm/V, compared with the performance of ordinary structured PCF at 20 ℃.

2. Models and theories

Fig. 1 shows the proposed multifunctional optoelectronic device based on LC selectively filled flat-plate PCF. The cladding has three layers of lattice-arranged air holes after being polished up and down, the duty ratio Λ is 7.9 μm, the air hole diameter d is 3.6 μm, and the thickness of the plate h is 18 μm. Unless otherwise specified, subsequent analyses are mainly based on these geometric parameters. The background material of the PCF is silica. A layer of nanofilm with a thickness of 40 nm is set inside the air hole A and filled with nematic liquid crystal (NLC) [33]. The two planes of the optical fiber are deposited with a gold nanofilm layer having a thickness of 40 nm as electrodes. The Drude Lorentz model is used to obtain the permittivity of the gold nanolayer [34].

$$\varepsilon_{Au} = \varepsilon_{\infty} - \frac{\omega_D^2}{\omega^2 + i\omega\gamma_D} - \frac{\triangle\varepsilon \cdot \Omega_L^2}{\left(\omega^2 - \Omega_L^2\right) + i\Gamma_L\omega}, \tag{1}$$

where ω is the angular frequency of transmitted light, ε_∞ is the permittivity and its value is 5.9673 when $\omega \to \infty$, ω_D is the plasma frequency ($\omega_D/2\pi = 2113.6$ THz), γ_D is the damping coefficient ($\gamma_D/2\pi = 15.92$ THz), Ω_L and Γ_L represent the oscillator strength and the spectral width of the Lorentz oscillators ($\Omega_L/2\pi = 650.07$ THz and $\Gamma_L/2\pi = 104.86$ THz) respectively, and $\Delta\varepsilon = 1.09$, which is the weighting factor.

NLC E7 is selected as the voltage-sensitive medium for the PCF; it has molecular orientation order and optical anisotropy. Under the condition of no electric field or voltage, the LC molecules in the holes are arranged in a plane, and the direction is parallel to the fiber axis [35]. Li et al. [36] studied the refractive indices n_e and n_o of the NLC under varying temperature and wavelength:

$$n_{eo} = A_{eo} + \frac{B_{eo}}{\lambda^2} + \frac{C_{eo}}{\lambda^4}, \tag{2}$$

where n_e is the extraordinary index and n_o is the ordinary RI, respectively, and A_e, B_e, C_e, A_o, B_o, and C_o are Cauchy coefficients that are sensitive to the temperature T. At $T = 20$ °C, the value of A_e, B_e, C_e, A_o, B_o, and C_o are 1.6993, 0.0085,0.0027, 1.4998, 0.0067, and 0.0004, respectively. The Cauchy coefficients at different temperatures can be obtained from [37]. Under the action of an external voltage, the LC produces an electro-optical effect, and the direction angle of the NLC molecules can be expressed as [38]:

$$\theta = \begin{cases} 0 & V \le Vc \\ \dfrac{\pi}{2} - 2\tan^{-1}\left[\exp\left(-\dfrac{V - Vc}{30Vc}\right)\right] & V > Vc \end{cases}, \tag{3}$$

where V_c is the threshold voltage, which is only related to the nature of the LC itself. When the external voltage is greater than the threshold voltage, the molecules begin to rotate. The rotation angle is close to 90° when the applied voltage reaches saturation. The RI of LC is closely related to the rotation angle, which can be expressed as [39]:

$$n = \frac{n_e n_0}{\sqrt{n_e^2\cos^2\theta + n_0^2\sin^2\theta}}, \tag{4}$$

Based on the characteristic that the RI of the LC can be controlled using the voltage, the LC is filled into the air holes of the PCF cladding, the change in the voltage leads to a change in the transmission characteristics of the PCF, thus realizing voltage sensing [40]. According to the definition, the voltage sensitivity can be expressed as:

$$Sv = \frac{\Delta\lambda_{res}}{\Delta V}, \tag{5}$$

where λ_{res} represents the resonance wavelength of the flat-plate PCF, V represents the applied voltage. In addition, the confinement loss can be expressed as follows [41]:

$$\alpha = 8.686 \times \frac{2\pi}{\lambda} \times \mathrm{Im}\left(n_{eff}\right). \tag{6}$$

where λ represents the light wavelength, another, $\mathrm{Im}(n_{eff})$ is expressed as the imaginary part of the effective RI of the waveguide mode.

There, commercial PCF (ESM-12, NKT Photonics) with hexagonal structure is used in our model. The fabrication of PCF mainly involves two processes: fabrication of PCF prefabricated rod and the PCF prefabricated rod is pulled to make PCF. In order to fabricate the flat-plate PCF structure with selective filling of LC, our entire process mainly includes LC filling, bilateral polishing and preparation of electrodes. Firstly, one end of the PCF is fused with the single-mode fiber, and the microscope-assisted cutting technique is used to cut the single-mode fiber at a distance of 10 μm from the melting point. The purpose is to seal all the air holes of the PCF with a fiber thin slice, so that the position of the air holes can be observed from the end of the fiber. Femtosecond laser micromachining technology is used to selectively drill holes at the end of the sealed PCF to open the air holes to be filled. One end of the PCF mold was put into the filling solution to achieve selective filling of the PCF air holes. After the filling process is complete, the PCF is inserted between two single-mode fibers and secured with a pair of fiber brackets. In this optical polishing system, the grinding wheel is fixed on a three-dimensional mechanical platform that can move in X, Y and Z directions. The polishing depth and length can be set by computer program. We use air laid paper with water to gently clean the polished surface of PCF to remove residual silica dust. Then the single side polishing process stops when the polishing surface appears near the PCF core area and the power loss in air is about 3 dB. Then, the two sides of the PCF are polished by using a clamp which is composed of a base composed of a three-dimensional displacement platform and optical fiber precision rotary clamping parts. Finally, magnetron sputtering coating technology and femtosecond laser processing technology were used to fabricate parallel plate electrode on the upper and lower lapping surface of flat-plate PCF, and DC source voltage was applied at both ends of the electrodes.

3. Simulation results and analysis

3.1. Filtering characteristics and voltage sensing characteristics

First, we studied the influence of the plate thickness on the photoelectric properties of the flat-plate PCF selectively filled with the LC. To eliminate the influence of temperature, the tentative ambient temperature in this study was set to 20 ℃. Fig. 2(a) depicts the confinement loss spectrum of the fundamental mode of the fiber core at different wavelengths at the time when $\Lambda = 7.9$ μm, $d = 3.6$ μm, and $h = 18$ μm under applied voltages of 200 and 600 V. As we can get from Fig. 2(a), with the increase of light wavelength, the core fundamental mode loss presents a trend of first increasing and then decreasing. In case of $V = 600$ V, when the fundamental mode of the fiber core and LC filling mode reach the phase matching condition, the constraint loss of the core fundamental mode reaches maximum at a wavelength λ = 941 nm, and the filter bandwidth at this time is approximately 100 nm. By

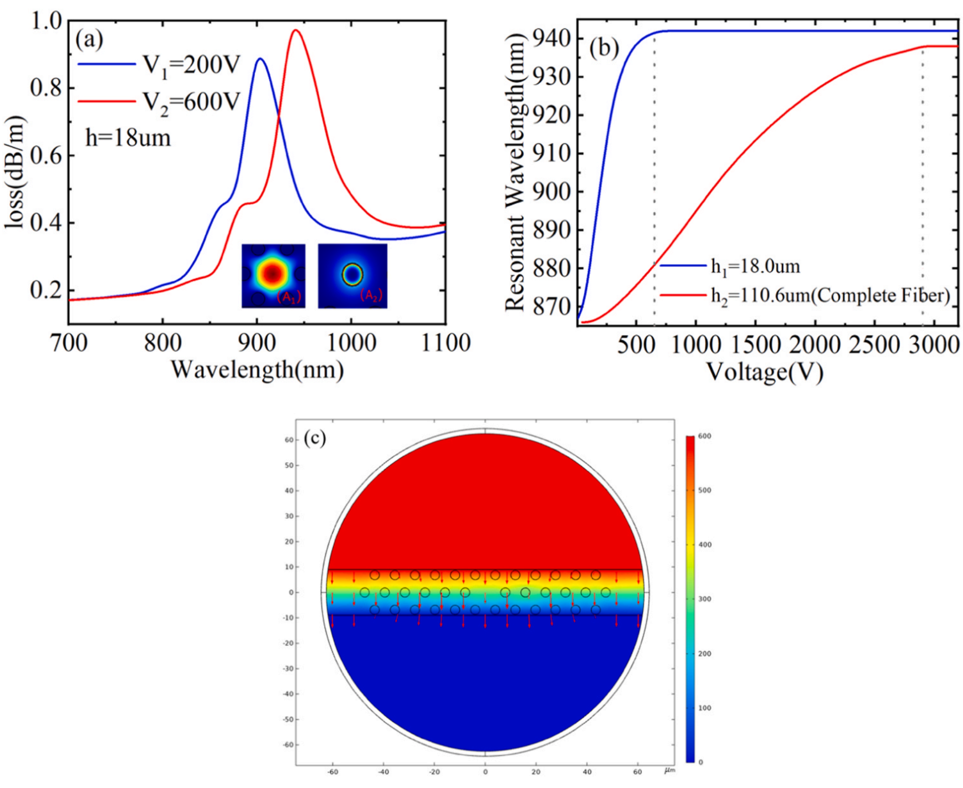

Fig. 2. (a) Loss spectrum of the core fundamental mode of the flat-plate photonic crystal fiber selectively filled with LC at $V_1 = 200$ V and $V_2 = 600$ V. (b) Relation diagram of the resonant wavelength with voltage when $h_1 = 18$ μm and $h_2 = 110.6$ μm. (c) Electric field distribution diagram when $h = 18$ μm and $V = 600$ V.

comparison, we find that when the applied voltage is increased from 200 to 600 V, the filter bandwidth remains unchanged, the loss peak redshifts, moreover, the loss peak value increases, which is because of the increase in the light energy absorbed by the LC molecules. To be more specific regarding this physical phenomenon, the mode field distribution diagram of these two modes which are fiber core fundamental mode and the filled LC mode respectively when the resonant wavelength $\lambda = 941$ nm is intercepted in this study, as illustrated in Fig. 2(a). The two modes are fully coupled when $\lambda = 941$ nm. Fig. 2(b) shows the variation curve of the resonance wavelength with the voltage drift when the coupling effect occurs in the air hole A. Evidently, when $h = 18$ μm and the voltage is in the range of 8–650 V, the resonance wavelength is more sensitive to the change in the voltage with good linearity, and the voltage sensitivity reaches 0.117 nm/V, moreover, the threshold voltage is lowered to 8 V. The threshold voltage can be described as the voltage value at which a linear wavelength shift occurs. When the applied voltage is lower than this threshold, the LC molecular alignment changes irregularly with the increase of voltage, resulting in irregular changes in RI, which produces a nonlinear shifts in the resonance wavelength of the device spectrum. For voltages above this threshold, linear wavelength shifts can be obtained [10]. As the voltage continues to increase, the resonance wavelength no longer changes. At this time, the deflection angle θ of the LC is 90°, and the external voltage reaches saturation at 650 V. At the same time, we can observe that with the increase in the voltage from 8 to 650 V, the resonance wavelength shifts from the initial 867–942 nm, and the tunable filter range is calculated as 75 nm. By comparison, when the structure is still a complete PCF, that is, $h = 110.6$ μm, the variation trend in the resonance wavelength with the voltage is the same as that when $h = 18$ μm, while the external voltage reaches saturation at 2900 V, and the voltage sensitivity is significantly reduced. Fig. 2(c) shows the electric field distribution when $h = 18$ μm and $V = 600$ V. The voltage of the plate decreases gradually from top to bottom; thus, the voltage of the air hole A can be calculated. Since the change in the RI of LC will lead to a sensitive change in the value of λ_{res}, when the RI of LC changes, which can be analyzed by comparing the shift in the resonance wavelength λ_{res}, voltage sensing can be realized. At the same time, the function of filtering can be achieved, and the modulation voltage of the filter can be reduced.

A resonance peak will appear at λ_{res} of the loss spectrum of the fiber core mode because the energy of the fundamental mode of the fiber core is partly transferred to the filling mode [42]. The plate thickness has a significant effect on the phase matching of these two modes. As the plate thickness changes, the resonance wavelength drifts accordingly. Therefore, the loss peak varies with the plate thickness.

Fig. 3(a) illustrates the loss spectrum of the fundamental mode of the fiber core under three different plate thicknesses when $V = 600$ V. These corresponding resonance wavelengths λ_{res} are 941, 927, and 908 nm, and the filtering bandwidths are 100, 60, and 60 nm, respectively. As the results shown from Fig. 3(a), we find that as the plate thickness decreasing, the resonance wavelength λ_{res} of the loss spectrum is red-shifted; on the other hand, the coupling strength between these two modes increases accordingly. In addition, when the plate thickness h is in the range of 18–46 μm, the resonance wavelength λ_{res} shifts from 941 to 908 nm; therefore, the adjustable wavelength range is 33 nm. To obtain the influence of the plate thickness on the photoelectric characteristics of the PCF more specifically, supplementary explanations are provided in Fig. 3(b), (c), and (d). Fig. 3(b) illustrates the variation curve of the

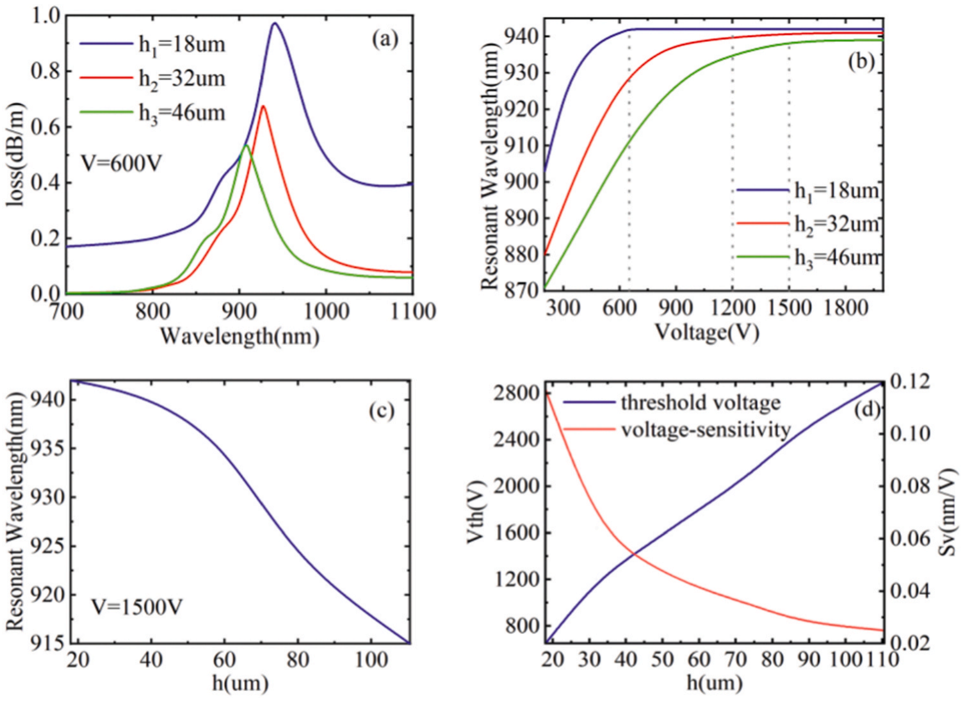

Fig. 3. (a) Loss spectrum of the core fundamental mode with $h = 18$, 32, and 46 μm when $\Lambda = 7.9$ μm, $d = 3.6$ μm, and $V = 600$ V. (b) Relation diagram of the resonance wavelength with voltage in the case of three different plate thicknesses. (c) Relationship between the resonance wavelength and the plate thickness when $V = 1500$ V. (d) Saturation voltage and average voltage sensitivity at different plate thicknesses.

resonance wavelength λ_{res} with voltage shift under three different plate thicknesses when $V = 600$ V, where the slope of the curve represents the voltage sensitivity. As the results shown from Fig. 3(b), as the plate thickness decreases from 46 to 18 μm, the saturation voltage decreases from 1500 to 650 V, and the voltage sensitivity increases. Fig. 3(c) depicts the curve of the resonance wavelength with the plate thickness when $V = 1500$ V. Evidently, when h decreases gradually, the resonance wavelength first presents a linear transformation and then gradually approaches saturation, which is consistent with the change rule shown in Fig. 3(b). Fig. 3(d) shows the saturation voltage V_{th} (left axis) and the average voltage sensitivity S_v (right axis) of the plate thickness in the range of 18–110.6 μm. From Fig. 3(d), we find that when the plate thickness is gradually reduced, the saturation voltage drastically reduces from 2900 to 650 V, and the relationship is linear. On the other hand, with the gradual decrease in the plate thickness, the voltage sensitivity first shows a slower increasing trend and then increases sharply. The voltage sensitivity increases from the initial 0.025 nm/V to 0.117 nm/V. The simulation results show that the modulation voltage of the filter can be effectively reduced by reducing the thickness of the plate, and the voltage sensing sensitivity is also greatly increased.

Next, we discuss the influence of the structural parameters of the flat-plate PCF on the optical and electrical properties. The PCF is flexible in terms of the setting of the structural parameters. By changing the structural parameters, the filtering characteristics and voltage sensing characteristics of the flat-plate PCF with LC selective filling can be changed, thereby optimizing its performance. The plate thickness below is set to 18 μm.

When the value of duty ratio Λ is set to 7.9 μm, the applied voltage V is set to 600 V, and the air hole diameter d is set to 3.4, 3.6, and 3.8 μm, respectively, the loss spectrum of the fundamental mode of the fiber core under three different air hole diameters is illustrated in Fig. 4(a). Evidently, due to the increase in air hole diameter gradually, we can get that the resonance wavelength λ_{res} of the loss spectrum is red-shifted. In addition, the peak loss decreases accordingly. This is because an increase in the air hole size results in a decrease in the equivalent RI of the cladding, and thus, an increase in the RI difference between the core and the cladding. As a result, the energy restriction ability of the core region becomes stronger, and finally, the loss of the guide mode of the core is reduced. In addition, when the air hole diameter d increases from 3.4 to 3.8 μm, the bandwidth of the filter increases from 80 to 120 nm, and the resonance wavelength shifts from 933 to 948 nm; further, the tunable wavelength range is 15 nm. To determine the effect of the plate thickness on the photoelectric characteristics of the flat-plate PCF in more detail, Fig. 4(b) and (c) are presented in this paper as supplementary explanation. Fig. 4(b) describes the variation of resonance wavelength λ_{res} with voltage under three different air hole diameters when $V = 600$ V. The three curves are parallel, and the slope of the curve represents the voltage sensitivity. From Fig. 4(b), we find that changing the value of d does not affect the saturation voltage and also has little effect on the voltage sensitivity. These two results can be specifically seen in Fig. 4(c). As shown, when the air hole diameter increases from 3.4 to 3.8 μm, the saturation voltage

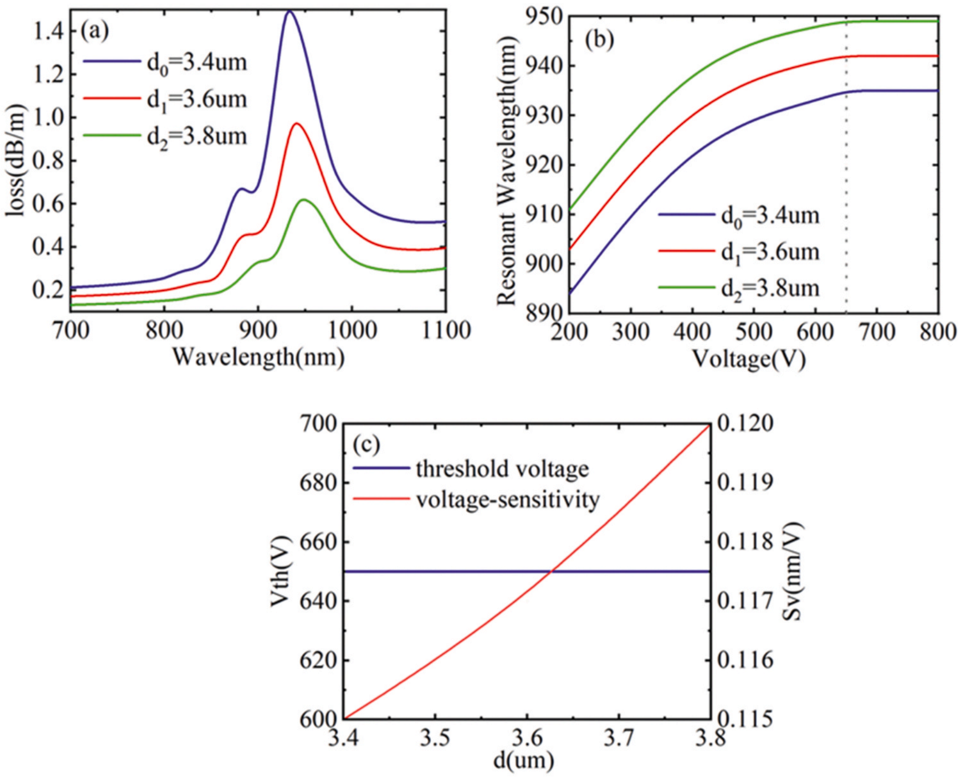

Fig. 4. (a) Loss spectrum of the core fundamental mode with d at 3.4, 3.6, and 3.8 μm when $\Lambda = 7.9$ μm and $V = 600$ V. (b) Relation diagram of the resonance wavelength with the voltage in the case of three different air hole diameters. (c) Saturation voltage and average voltage sensitivity at different air hole diameters.

remains unchanged at 650 V, and the voltage sensitivity increases linearly from 0.115 to 0.120 nm/V, with little difference. Therefore, optimizing the air hole diameter cannot help reduce the modulation voltage of the filter, and at the same time, the effect of improving the voltage sensitivity is small.

When discussing the influence of the diameter of the air hole A filled with LC on the optical and electrical characteristics of the flat-plate PCF, $\Lambda = 7.9$ μm, $d = 3.6$ μm, and $V = 600$ V remain unchanged, and the diameter of the air hole A is set to 2.6, 3.6, and 4.6 μm. Fig. 5(a) illustrates the loss spectrum under three diameter settings of the air hole A. With the increase in the diameter, the resonance wavelength λ_{res} is red-shifted; moreover, the peak value of the resonance loss increases accordingly. The reason is that an increase in the air hole A filled with LC will cause an increase in the real part of the effective RI of the mode in the waveguide A, which shifts the wave vector matching point of the fundamental mode of the fiber core and waveguide mode to the long wavelength direction. In addition, as the diameter of the air hole D increasing from 2.6 to 4.6 μm, the bandwidth of the filter remains unchanged at 100 nm; however, the resonance wavelength λ_{res} shifts from 892 to 967 nm; therefore, the tunable wavelength range is 75 nm. To understand the influence of the diameter of the air hole A on the photoelectric features of the flat-plate PCF more specifically, supplementary explanations are provided in Fig. 5(b) and (c). Fig. 5(b) describes the variation of resonance wavelength λ_{res} with voltage under three different diameters of the air hole A when $V = 600$ V. The three curves are parallel, and the slope of the curve represents the voltage sensitivity. As we can obtain from Fig. 5(b), when the diameters of the air hole A are 2.6, 3.6, and 4.6 μm, the corresponding saturation voltages are 850, 650, and 550 V, respectively. Thus, increasing the diameter can help reduce the saturation voltage and increase the voltage sensitivity. These two results can be specifically seen in Fig. 5(c). Fig. 5(c) shows the saturation voltage and average voltage sensitivity of the air hole A when the diameter ranges from 2.6 to 4.6 μm. With the increase in the diameter of the air hole A, the saturation voltage decreases from 850 to 550 V, and the voltage sensitivity increases from 0.080 to 0.145 nm/V. The two curves are linear. Therefore, the modulation voltage of the filter can be effectively reduced, and the voltage sensitivity can also be improved by optimizing the diameter of the air hole A.

Fig. 6(a) presents the loss spectrum of the fiber core fundamental mode, when the duty ratio is set to 7.7, 7.9, and 8.1 μm, respectively, and $d = D = 3.6$ μm, and $V = 600$ V. As demonstrated in Fig. 6(a), as Λ increases, the coupling efficiency between the fiber core mode and the filled mode increases. However, the position of the resonant wavelength is unaffected by the duty ratio. When Λ increases from 7.7 to 8.1 μm, the bandwidth of the filter increases from 90 to 110 nm, and the resonance wavelength λ_{res} remains unchanged at 941 nm. Therefore, the tunable function cannot be realized. Fig. 6(b) shows the effects of the duty ratio on the saturation voltage and voltage sensitivity. In Fig. 6(b), we find that the three curves corresponding to the three different duty ratios coincide, indicating that the saturation voltage and voltage sensitivity remain unchanged with the change in the duty ratio, that is, the saturation voltage $V_{th} = 650$ V and the voltage sensitivity $S_v = 0.117$ nm/V. Therefore, it is impossible to reduce the modulation voltage of the filter and increase the sensitivity of voltage by optimizing the value of Λ.

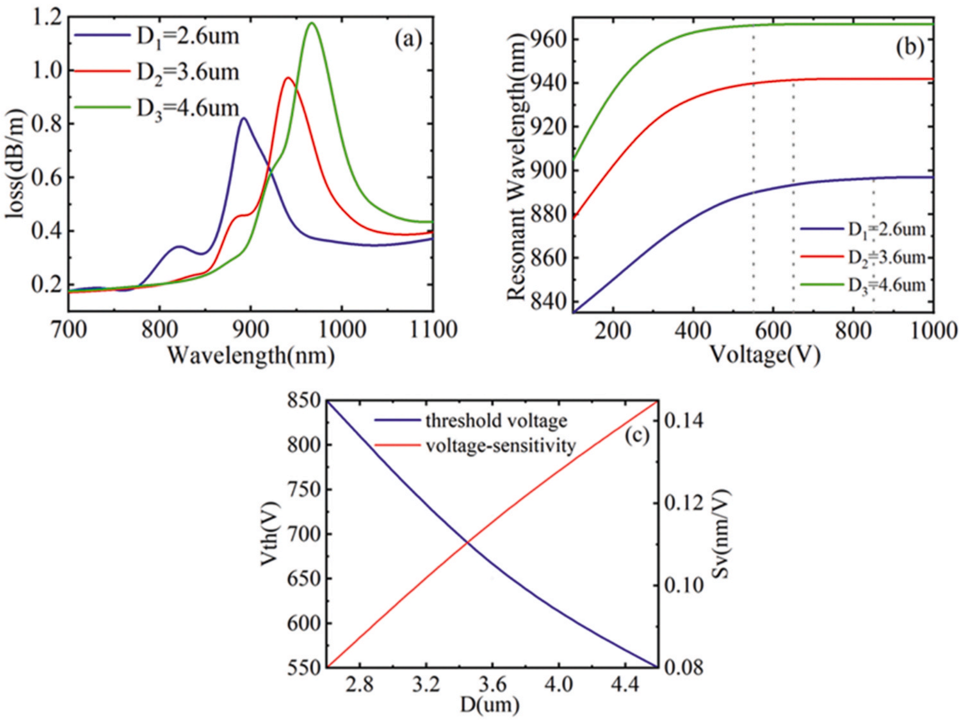

Fig. 5. (a) Loss spectrum of the core fundamental mode when $\Lambda = 7.9$ μm, $d = 3.6$ μm, and $V = 600$ V and when the diameter of the air hole A is set to 2.6, 3.6, and 4.6 μm, respectively. (b) Relation diagram of the resonance wavelength with the voltage in the case of three different diameters of the air hole A. (c) Saturation voltage and average voltage sensitivity under different diameters of the air hole A.

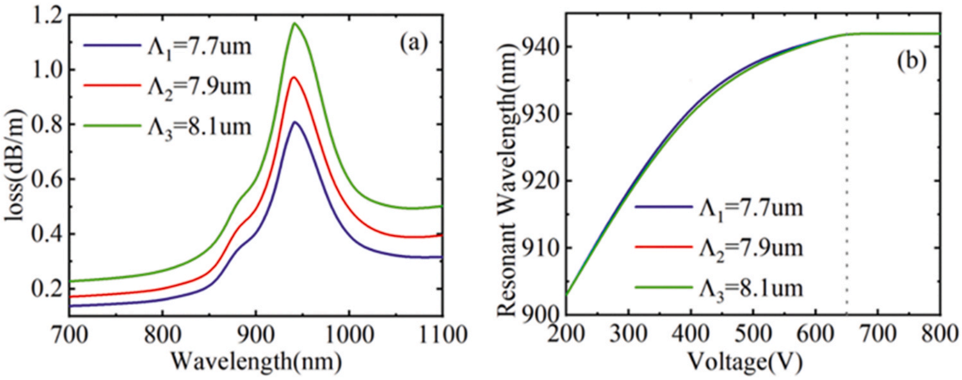

Fig. 6. (a) Loss spectrum of the core fundamental mode at duty ratios of 7.7, 7.9, and 8.1 μm when $d = D = 3.6$ μm and $V = 600$ V.(b) Relation diagram of the resonance wavelength with voltage under three different duty ratios.

Fig. 7(a) demonstrates the loss spectrum of the core fundamental mode when $V = 600$ V and when the thickness of the metal film t is set to be 35, 40, and 45 nm, respectively. As revealed in Fig. 7(a), when the metal film thickness t increases, the resonance wavelength λ_{res} appears red-shifted, and that the peak value of the resonance loss decreases accordingly. In addition, when t increases from 35 to 45 nm, we find that the bandwidth of the filter increases from 70 to 160 nm, the resonance wavelength drifts from 919 to 956 nm, and the tunable wavelength range is 37 nm. To determine the effect of the metal film thickness on the photoelectric properties of the flat-plate PCF more specifically, Fig. 7(b) and (c) are given in this paper as supplementary explanation. Fig. 7(b) shows the variation in the resonance wavelength λ_{res} with the voltage under three different metal film thicknesses when $V = 600$ V. The three curves are parallel, and the slope of the curve represents the voltage sensitivity. As shown in Fig. 7(b), changing the value of t does not affect the value of the saturation voltage and has little effect on the voltage sensitivity. These two results can be seen in detail in Fig. 7 (c). From Fig. 7(c), we find that as the thickness of the metal film t increases from 35 to 45 nm, the saturation voltage remains

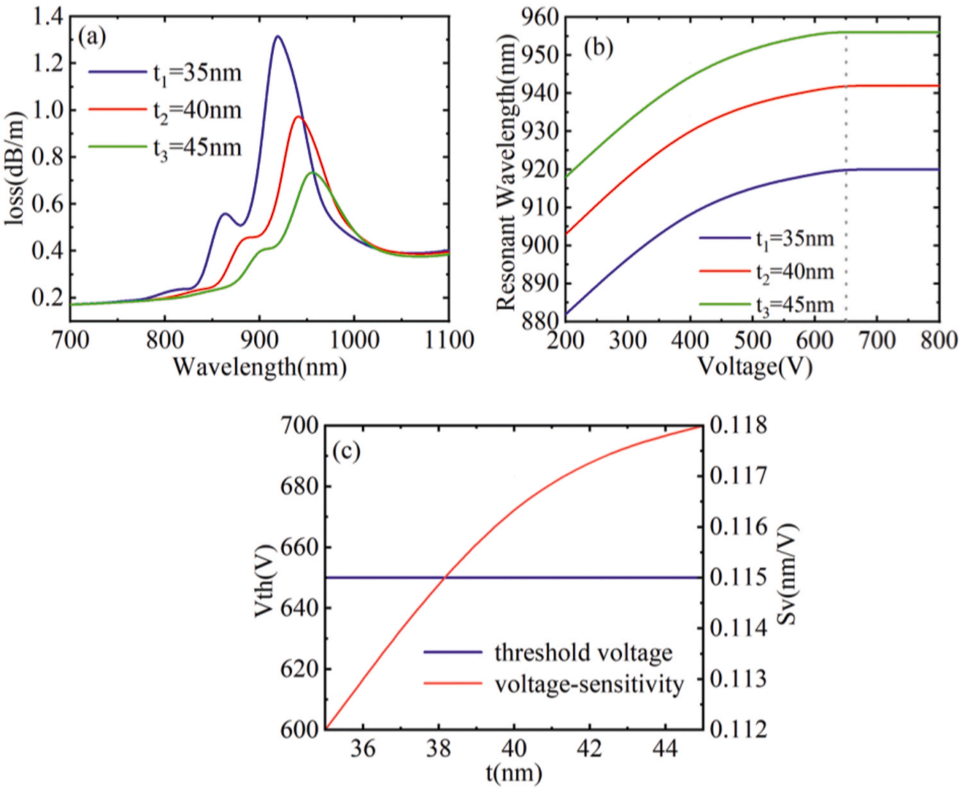

Fig. 7. (a) Loss spectrum of the core fundamental mode with the metal film thickness at 35, 40, and 45 nm when $\Lambda = 7.9$ μm, $d = 3.6$ μm, and $V = 600$ V. (b) Relation diagram of the resonance wavelength with the voltage in the case of three different metal film thicknesses. (c) Saturation voltage and average voltage sensitivity at different metal film thicknesses.

unchanged at 650 V, and the voltage sensitivity increases from 0.112 to 0.118 nm/V, with little change. Therefore, the modulation voltage of the filter cannot be reduced by optimizing the metal film thickness, and the effect of improving the voltage sensitivity is small, which is similar to the effect of adjusting the air hole diameter.

The n_e and n_o refractive indices of LCs are both temperature-dependent [33]. Therefore, the properties of the flat-plate PCF can be optimized from the outside rather than changing their geometry through virtue of their temperature-adjustable properties. Therefore, the effect of temperature change on the photoelectric properties of the flat-plate PCF was also studied in this work.

Fig. 8(a) reveals the loss spectrum of the core fundamental mode at every 5 ℃ in the temperature range of 15–50 ℃ when $h = 18$ μm and $V = 600$ V. As shown in Fig. 8(a), when the temperature T goes from 15° to 35°C, we obtained that the peak wavelength of the loss spectrum appears blue-shifted. Compared with that at $T = 35$ ℃, when T reaches 40 ℃, the peak wavelength suddenly moves to the long wavelength direction. In turn, when $T = 45$ ℃, the peak wavelength moves to the short wavelength direction, and when $T = 50$ ℃, the peak wavelength shifts to the long wavelength direction. What's more, the peak value of the resonance loss changes little. When $T = 15$, 25, 35, and 45 ℃, the corresponding resonance wavelengths λ_{res} are 947, 938, 929, and 939 nm, respectively. From these results, we can conclude that every 10 ℃ change in the temperature corresponds to a resonance wavelength change of approximately 9 nm. Therefore, the structure has an adjustable temperature sensitivity of approximately 0.9 nm/℃. The simulation results show that the resonance wavelength is temperature adjustable, i.e., by adjusting the temperature T of LC, the location of the resonance wavelength will be adjusted to our desired value. Hence, the structure studied in this paper is temperature adjustable. For a more detailed description of the influence of temperature on the optical and electrical characteristics of flat-plate PCFs, supplementary explanations are provided in Fig. 8(b) and (c). Fig. 8(b) depicts the variation in the resonance wavelength with the voltage at temperatures of 15, 20, and 25 ℃ when $V = 600$ V. The three curves have the same trend, and the slope of the curve represents the voltage sensitivity. As shown in Fig. 8(b), when the external voltage takes the minimum of 8 V, the resonance wavelengths in the three cases are the same; however, when saturation is reached at 650 V, the corresponding resonance wavelengths are significantly different. Therefore, the saturation voltage value is unaffected by the change in the temperature, whereas the voltage sensitivity decreases with increasing temperature. These two results can be specifically seen in Fig. 8(c). We find that the temperature is within the range of 15–50 ℃, the saturation voltage remains unchanged at 650 V, and the voltage sensitivity drops from 0.120 to 0.084 nm/V, as shown in Fig. 8(c). Therefore, adjusting the temperature cannot achieve the purpose of reducing the modulation voltage of the filter and improving the voltage sensitivity, but has the advantage of thermal adjustability.

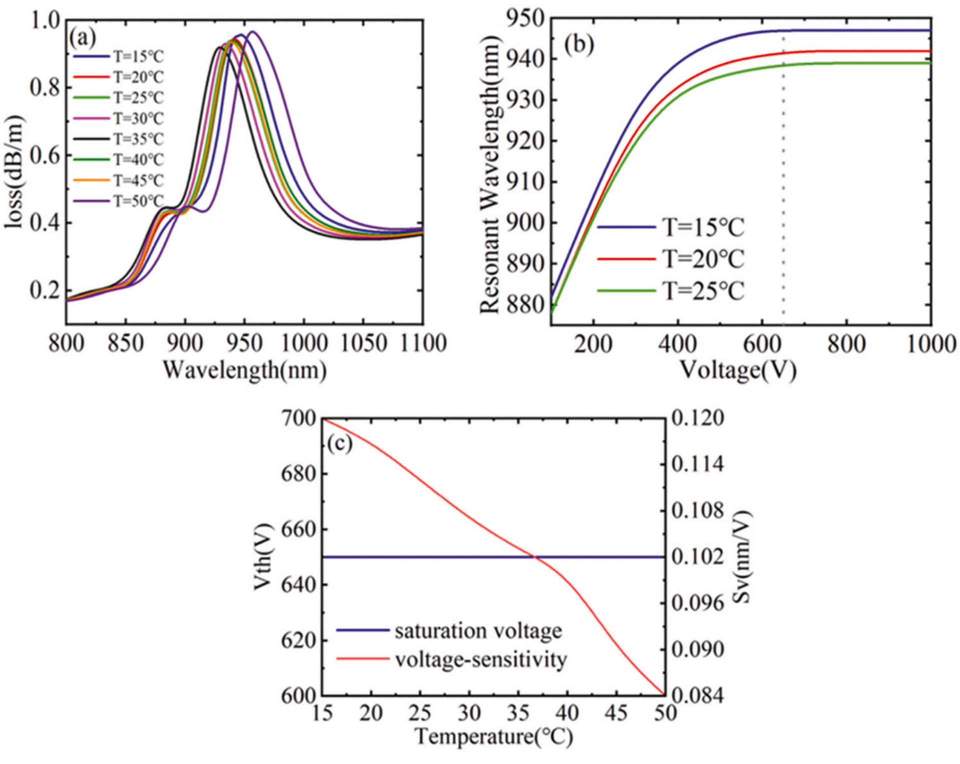

Fig. 8. (a) Loss spectrum of the core fundamental mode at different temperatures when $\Lambda = 7.9$ μm, $d = 3.6$ μm, $h = 18$ μm, and $V = 600$ V. (b) Relation diagram of the resonance wavelength with voltage when the temperature is set to 15, 20, and 25 ℃, respectively. (c) Saturation voltage and average voltage sensitivity at different temperatures.

3.2. Dual-parameter sensing of RI and voltage

Finally, considering the structural flexibility and performance advantages of flat-plate PCFs, we designed a physical model of the RI and voltage dual-parameter sensing for the flat-plate PCF based on the mode-coupling theory and the multi-physical field coupling finite element analysis method. The upper and lower plates are filled with the analysis liquid, and the RI of the measured object can be obtained by measuring the position of the peak wavelength, which is the theory of RI sensing.

Fig. 9(a) describes the loss spectra of the core fundamental mode at $V = 600$ V, and the value of RI of the sensing analyte is 1.32, 1.33, and 1.34, respectively. As shown in Fig. 9(a), when the other parameters are kept unchanged, the peak wavelength appears red-shifted when increasing the value of RI gradually, while the coupling strength decreases accordingly, as indicated by peak1. This is because surface plasmon resonance is closely related to the RI of the surrounding environment. When the RI increases initial from 1.32 to 1.33 and then to 1.34, we can get that the change in the peak wavelength $\Delta\lambda_{\text{res}}$ is calculated as 16 nm. Additionally, the change of the RI does not affect the position of peak2, which not only has a greater absorption intensity but is also narrower. Similarly, as revealed in Fig. 9(b), when the value of RI remains unchanged at 1.33, and only the external voltage is changed, the position of peak1 remains unchanged, while the position of peak2 appears red-shifted as the external voltage increases, and the coupling strength increases accordingly. This is because a change in the external voltage affects the RI of the LC, which affects the effective RI of the coupled waveguide mode. At the same time, the peak wavelength shift when the external voltage increases from 200 to 400 V is significantly greater than that when the external voltage increases from 400 to 600 V, which can be specifically analyzed in Fig. 9(d). In summary, the two loss peaks do not affect each other; thus, we can better distinguish the two sensing mechanisms and achieve a simultaneous sensing of the voltage and RI. Fig. 9(c) shows the resonance wavelength λ_{res} as a function of the RI of the sensing analyte, where the slope of the curve represents the RI sensitivity. As the RI varies from 1.32 to 1.40, the resonance wavelength shifts to the long wavelength direction with the increase in the RI, and the relationship is linear. The peak wavelength and RI meet the following condition: $\lambda = 2700\ n - 2944$, i.e., the RI sensitivity is 2700 nm/RIU. The refractive index resolution (R) of the proposed device can be defined as $R = \Delta n_{\text{a}}\ \Delta\lambda_{\min}\ /\ \Delta\lambda_{\text{res}}$ [43], whose value is calculated as $3.7\text{x}10^{-5}$ RIU. The detection limit (DL) is determined by its RI sensitivity and sensor resolution by $\text{DL} = R\ /\ S$ [44]. The value of DL of our sensor is $1.37\text{x}10^{-8}$. Fig. 9(d) illustrates the diagram of the relationship between the peak wavelength of the core fundamental mode and the external voltage. Similar to that obtained from Fig. 2 (b), when the value of V is in the range of 100–900 V with $n = 1.33$, the resonance wavelength changes with the voltage more sensitive, and the linearity is good. As the voltage continues to increase, the resonance wavelength remains unchanged, and the external voltage reaches saturation at 900 V. The slope of the curve represents the voltage sensitivity. As shown in Fig. 9(d), the linearity of the voltage in the range of 200–400 V is better than that in the range of 400–600 V, and the resonance wavelength is more sensitive to the change in the voltage. In summary, the RI and voltage measurements of the device are independent of each other, thus realizing a simultaneous measurement of the two parameters.

4. Conclusions

In conclusion, we proposed and numerically analyzed a multifunctional optical device based on a section of flat-plate PCF selectively filled with LC. The device has the following three functions: (1) Silica is a nonpolarized material, so the plate structure can effectively reduce the modulation voltage. As a fiber filter, the applied saturation voltage decreases from 2900 V (ordinary structure) to 650 V; (2) Based on the relationship between the coupling wavelength of the core waveguide mode and the filled mode and the applied voltage, this structure can realize the sensing of the external voltage and the intensity of the environmental electric field. As a voltage sensor, the voltage sensitivity is improved from 0.025 to 0.117 nm/V. (3) the metal film is close enough to the fiber core to enable coupling between the core waveguide mode and the surface plasmon resonance mode. Thus, the environmental RI can be measured. The independent detection function of RI and voltage makes it can be used as a dual-parameter sensor. Hence, flat-plate PCFs based on the selective filling of LCs has the potential for a wide range of applications.

Funding

National Natural Science Foundation of China (61805051); Natural Science Foundation of Guangxi Province (2018JJB170035, 2018AD19071, 2019GXNSFFA245002, 2020JJA170047, 2018GXNSFAA281305, AD18281060); Dean Project of Guangxi Key Laboratory of Wireless Broadband Communication and Signal Processing (GXKL06190118, GXKL06160102, GXKL06180104).

Disclosures

The authors declare no conflicts of interest.

Declaration of Competing Interest

The authors declare that they have no known competing financial interests or personal relationships that could have appeared to influence the work reported in this paper.

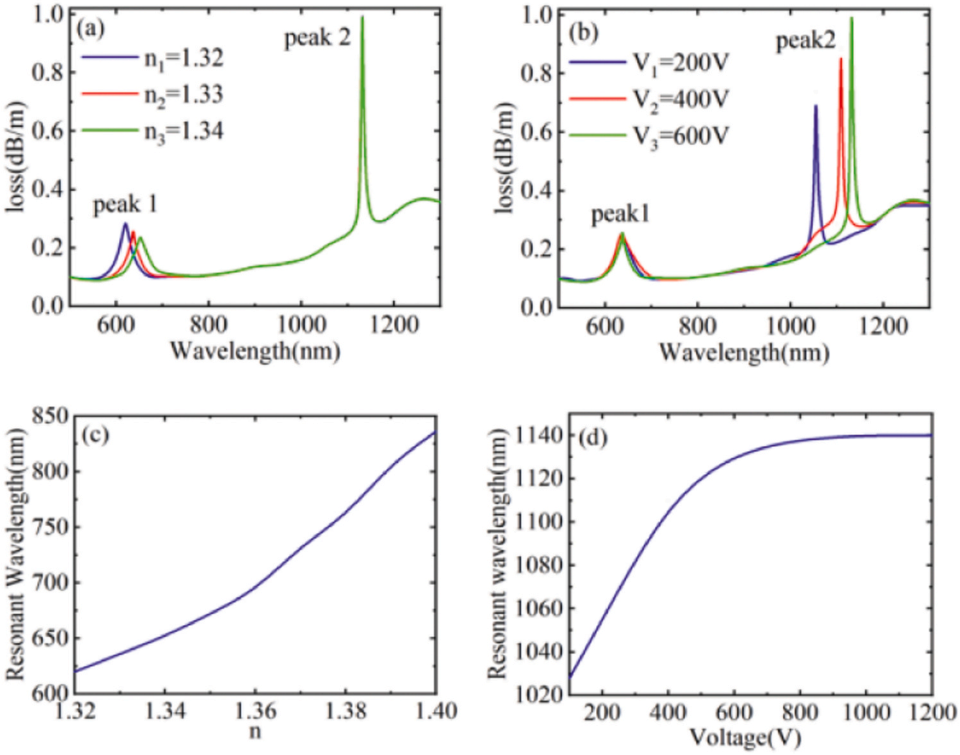

Fig. 9. (a) Loss spectrum of the core fundamental mode with three refractive indices of the sensing analyte when $\Lambda = 7.9$ μm, $d = 3.6$ μm, and $V = 600$ V. (b) Loss spectrum of the core fundamental mode at external voltages of 200, 400, and 600 V when $n = 1.33$. (c) Relation diagram of the resonance wavelength with the RI when the refraction index of the sensing analyte is in the range of 1.32–1.40. (d) Relation diagram of the resonance wavelength with the external voltage when the external voltage is in the range of 100–1200 V.

Data availability

Data underlying the results presented in this paper are not publicly available at this time but may be obtained from the authors upon reasonable request.

References

[1] R.C. Jorgenson, S.S. Yee, A fiber optic chemical sensor based on surface plasmon resonance, Sens. Actuators B Chem. 12 (3) (1993) 213–220.
[2] Mohamed Farhat O. Hameed, A.M. Heikal, B.M. Younis, Maher Abdelrazzak, S.S.A. Obayya, Ultra-high tunable liquid crystal-plasmonic photonic crystal fiber polarization filter, Opt. Express 23 (6) (2015) 7007–7020.
[3] A. Chen, Z. Yu, B. Dai, Y. Li, Highly sensitive detection of RI and temperature based on liquid-filled D-shape PCF, IEEE Photonics Technol. Lett. 33 (11) (2021) 529–532.
[4] J. Tang, Z. Xiao, K. Xu, Ultra-thin metamaterial absorber with extremely bandwidth for solar cell and sensing applications in visible region, Opt. Mater. 60 (2016) 142–147.
[5] T.R. Wolinski, A. Czapla, S. Ertman, M. Tefelska, Andrzej W. Domanski, Edward Nowinowski-Kruszelnicki, Dabrowski Roman, Tunable highly birefringent solid-core photonic liquid crystal fibers, Opt. Quantum Electron. 39 (12–13) (2007) 1021–1032.
[6] Y. Guo, J.S. Li, S.G. Li, Y.C. Liu, X.J. Meng, W.H. Bi, H.B. Lu, T.L. Cheng, R. Hao, Amphibious sensor of temperature and RI based on D-shaped photonic crystal fiber filled with liquid crystal, Liq. Cryst. 47 (6) (2020) 882–894.
[7] A. Siarkowska, M. Chychlowski, D. Budaszewski, B. Jankiewicz, B. Bartosewicz, T.R. Wolinski, Thermo- and electro-optical properties of photonic liquid crystal fibers doped with gold nanoparticles, Beilstein J. Nanotechnol. 8 (2017) 2790–2801.
[8] G. Ren, P. Shum, X. Yu, J. Hu, G. Wang, Y. Gong, Polarization dependent guiding in liquid crystal filled photonic crystal fibers, Opt. Commun. 281 (6) (2008) 1598–1606.
[9] L. Yu, L. Chen, W.G. Zhang, Y.S. Zhang, S. Wang, Y.X. Zhang, T.Y. Yan, J. Yang, Ultrashort polarization rotator based on spiral photonic crystal fiber aided by liquid crystal, Appl. Opt. 56 (25) (2017) 7294–7298.
[10] Y.J. Huang, Y. Wang, L.F. Zhang, Y. Shao, F. Zhang, C.R. Liao, Y.P. Wang, Tunable electro-optical modulator based on a photonic crystal fiber selectively filled with liquid crystal, J. Light. Technol. 37 (9) (2019) 1903–1908.
[11] L.H. Jiang, G.X. Zhang, Y.Y. Zhang, J.H. Zou, C. Wang, Y.F. Qi, L.T. Hou, A miniaturized and high-bandwidth polarization filter based on a plasmonic and liquid crystal offset core photonic crystal fiber, Opt. Quantum Electron. 52 (9) (2020) 409.
[12] X.Q. Liu, Y.G. Liu, Z. Wang, Double telecom band thermo-optic switch based on dual-line filled photonic liquid crystal fibres, Liq. Cryst. 44 (3) (2017) 479–483.
[13] X.P. Luo, F.R. Wang, C.L. Chen, L.L. Zhang, L. Wang, W.M. Sun, Y.J. Liu, A novel mach-zehnder interferometer based on hybrid liquid crystal-photonic crystal fiber, Chin. Phys. Lett. 34 (12) (2017).
[14] D.J.J. Hu, J.L. Lim, Y. Cui, K.L. Milenko, Y.X. Wang, P.P. Shum, T. Wolinski, Fabrication and characterization of a highly temperature sensitive device based on nematic liquid crystal-filled photonic crystal fiber, IEEE Photonics J. 4 (5) (2012) 1248–1255.

[15] M. Fokine, L.E. Nilsson, A. Claesson, D. Berlemont, L. Kjellberg, L. Krummenacher, W. Margulis, Integrated fiber Mach-Zehnder interferometer for electro-optic switching, Opt. Lett. 27 (18) (2002) 1643–1645.
[16] Z.W. Yu, W. Margulis, O. Tarasenko, P.Y. Fonjallaz, Nanosecond switching of fiber Bragg gratings, Opt. Express 15 (22) (2007) 14948–14953.
[17] L.H. Jiang, Y. Zheng, J.J. Yang, L.T. Hou, Z.H. Li, X.T. Zhao, An ultra-broadband single polarization filter based on plasmonic photonic crystal fiber with a liquid crystal core, Plasmonics 12 (2) (2017) 411–417.
[18] C.K. Yang, H. Zhang, B. Liu, S.W. Lin, Y.T. Li, H.F. Liu, Electrically tunable whispering gallery mode microresonator based on a grapefruit-microstructured optical fiber infiltrated with nematic liquid crystals, Opt. Lett. 42 (15) (2017) 2988–2991.
[19] M.Y. Azab, M.F.O. Hameed, S.S.A. Obayya, Multi-functional optical sensor based on plasmonic photonic liquid crystal fibers, Opt. Quantum Electron.. 49 (2) (2017) 49.
[20] M.H. Tatiana, R.V. Erick, T. Pedro, Tunable whispering gallery mode photonic device based on microstructured optical fiber with internal electrodes, Sci. Rep. 9 (2019) 12083.
[21] J.A.M. Cardona, N.D.G. Cardona, E.G. Valencia, P.T. Trujillo, E.R. Vera, Tunable mode converter device based on photonic crystal fiber with a thermo-responsive liquid crystal core, Photonics 7 (1) (2020) 3.
[22] Q.J. Lu, X.G. Chen, X.L. Liu, L. Fu, C.L. Zou, S.S. Xie, Tunable optofluidic liquid metal core microbubble resonator, Opt. Express 28 (2) (2020) 2201–2209.
[23] S.M.H. Abdelaal, B.M. Younis, S.S.A. Obayya, M.F.O. Hameed, Highly negative dispersion dual-core liquid crystal photonic crystal fiber, Opt. Fiber Technol. 60 (2020), 102330.
[24] G.C. Nelson, J.D. Cristian, U.R. Juan, T. Pedro, R.V. Erick, Thermo-optically tunable polarization beam splitter based on selectively gold-filled dual-core photonic crystal fiber with integrated electrodes, Opt. Quantum Electron. 53 (2) (2021) 68.
[25] M.M.H. Mahmoud, B.M. Younis, N.F.F. Areed, M.F.O. Hameed, S.S.A. Obayya, Tunable liquid crystal asymmetric dual-core photonic crystal fiber mode converter, Appl. Opt. 60 (25) (2021) 7671–7677.
[26] S. Tian, T.Y. Yang, J.X. Zhang, K. Xie, J.J. Ma, L. Hong, Y.H. Luo, Z.J. Hu, Multi-band thermal optical switch based on nematic liquid crystal filled photonic crystal fiber, J. Light. Technol. 39 (10) (2021) 3297–3302.
[27] G.W. An, S.G. Li, W. Qin, W. Zhang, Z.K. Fan, Y.J. Bao, High-sensitivity RI sensor based on D-shaped photonic crystal fiber with rectangular lattice and nanoscale gold film, Plasmonics 9 (6) (2014) 1355–1360.
[28] H.L. Chen, S.Q. Li, G.W. An, J.S. Li, Z.K. Fan, Y. Han, Polarization splitter based on d-shaped dualcore photonic crystal fibers with gold film, Plasmonics 10 (1) (2015) 57–61.
[29] J.N. Dash, R. Jha, Highly sensitive D shaped PCF sensor based on SPR for near IR, Opt. Quantum Electron. 48 (2) (2016) 137.
[30] C. Liu, W.Q. Su, Q. Liu, X.L. Lu, F.M. Wang, T. Sun, P.K. Chu, Symmetrical dual D-shape photonic crystal fibers for surface plasmon resonance sensing, Opt. Express 26 (7) (2018) 9039–9049.
[31] T.S. Wu, Y. Shao, Y. Wang, S.Q. Cao, W.P. Cao, F. Zhang, C.R. Liao, J. He, Y.J. Huang, M.X. Hou, Y.P. Wang, Surface plasmon resonance biosensor based on gold-coated side-polished hexagonal structure photonic crystal fiber, Opt. Express 25 (17) (2017) 20313–20322.
[32] Q. Liu, P.S. Xue, Z.Y. Liu, Voltage sensor based on liquid-crystal-infiltrated photonic crystal fiber with high index, Appl. Phys. Express 13 (3) (2020), 032005.
[33] T.R. Wolinski, A. Czapla, S. Ertman, M. Tefelska, A.W. Domanski, J. Wojcik, E. Nowinowski-Kruszelnicki, R. Dabrowski, Photonic liquid crystal fibers for sensing applications, IEEE Trans. Instrum. Meas. 57 (8) (2008) 1796–1802.
[34] X. Chen, W.Y. Bu, Z.F. Wu, H.J. Zhang, P.P. Shum, X.G. Shao, J.X. Pu, Near-infrared long-range surface plasmon resonance in a D-shaped honeycomb microstructured optical fiber coated with Au film, Opt. Express 29 (11) (2021) 16455–16468.
[35] M.W. Haakestad, T.T. Alkeskjold, M.D. Nielsen, L. Scolari, J. Riishede, H.E. Engan, A. Bjarklev, Electrically tunable photonic bandgap guidance in a liquid-crystal-filled photonic crystal fiber, IEEE Photonics Technol. Lett. 17 (4) (2005) 819–821.
[36] J. Li, S.T. Wu, S. Brugioni, R. Meucci, S. Faetti, Infrared refractive indices of liquid crystals, J. Appl. Phys. 97 (7) (2005).
[37] H. Liu, C.H. Zhu, Y. Wang, C. Tan, H.W. Li, Polarization-dependent transverse-stress sensing characters of the gold-coated and liquid crystal filled photonic crystal fiber based on Surface Plasmon Resonance, Opt. Fiber Technol. 41 (2018) 27–33.
[38] E.L. Wang, H.M. Jiang, K. Xie, C. Chen, Z.J. Hu, Polarization splitter based on dual core liquid crystal-filled holey fiber, J. Appl. Phys. 120 (11) (2016), 114501.
[39] K.R. Khan, K. Mnaymneh, H. Awad, I. Hasan, Slow light propagation in tunable nanoscale photonic crystal cavity filled with nematic liquid crystal, Opt. Eng. 53 (10) (2014), 102705.
[40] H.L. Chen, S.G. Li, M.J. Ma, J.S. Li, Z.K. Fan, M. Shi, Surface plasmon induced polarization filter based on au wires and liquid crystal infiltrated photonic crystal fibers, Plasmonics 11 (2) (2016) 459–464.
[41] H.L. Chen, S.G. Li, M.J. Ma, Z.K. Fan, Y.D. Wu, Ultrabroad bandwidth polarization filter based on D shaped photonic crystal fiber with gold film, Plasmonics 10 (5) (2015) 1239–1242.
[42] K. Saitoh, M. Koshiba, Full-vectorial imaginary-distance beam propagation method based on a finite element scheme: Application to photonic crystal fibers, IEEE J. Quantum Electron. 38 (7) (2002) 927–933.
[43] C. Liu, F.M. Wang, J.W. Lv, T. Sun, Q. Liu, H.W. Mu, P.K. Chu, Design and theoretical analysis of a photonic crystal fiber based on surface plasmon resonance sensing, J. Nanophotonics 9 (2015).
[44] N. Zhang, G. Humbert, Z.F. Wu, K.W. Li, P.P. Shum, N.M.Y. Zhang, Y. Cui, J.L. Auguste, X.Q. Dinh, L. Wei, In-line optofluidic refractive index sensing in a side-channel photonic crystal fiber, Opt. Express 24 (24) (2016) 27674–27682.